Article

Epithermal origin and environmental evolution of iron-hosted thallium and kerogen deposits: The Lodares area case (Soria, Spain)

Javier Garcia-Guinea[1,*], Fernando Garrido[1], Paula Lopez-Arce[1], Andreas Voegelin[2], Jörg Göttlicher[3], Stephan Mangold[3], Gonzalo Almendros[1]

[1,*] Museo Nacional de Ciencias Naturales (CSIC), C/ José Gutiérrez Abascal 2, 28026-Madrid;
[2]Eawag, Swiss Federal Institute of Aquatic Science and Technology, Department of Water Resources and Drinking Water, Überlandstrasse 133, CH-8600 Dübendorf (Switzerland)
[3]Karlsruhe Institute of Technology, Institute for Photon Science and Synchrotron Radiation, KIT Campus North, Hermann-von-Helmholtz-Platz 1, D-76344 Eggenstein-Leopoldshafen (Germany)
Javier.Garcia.Guinea@csic.com; Fernando.Garrido@mncn.csic.es; plopezarce@mncn.csic.es; andreas.voegelin@eawag.ch; joerg.goettlicher@kit.edu; stefan.mangold@kit.edu; humus@mncn.csic.es;
Tel.: +00-34-914111328

Academic Editor: Cristian Biagioni
Received: date; Accepted: date; Published: date

Abstract: Hydrothermal pyrite is an important source of thallium (Tl) but this rare element can be also detected in the secondary iron goethite-lepidocrocite and jarosite ores, associated to hydrothermal kerogen, manganese oxides, accessorial potassium minerals and tiny Tl-bearing clusters shielded in quartz masses. We studied Tl-bearing samples collected from Fe-Mn ores hosted in dolostone rocks sited along ca. 15 km of fossil thermal springs following a geological fault in the Lodares surroundings. Samples were analyzed by environmental scanning electron microscopy and energy dispersive spectroscopy (ESEM-EDS), electron probe micro-analysis (EPMA), inductively coupled plasma-mass spectroscopy (ICP-MS), X-ray diffraction analysis (XRD), Tl L_{III}-edge X-ray absorption near-edge structure (XANES) spectroscopy, Micro-Raman and Fourier transform infrared spectroscopy (FTIR). We found epithermal pyrite, sphalerite, galena and baryte and secondary gypsum, jarosite, scorodite, anglesite, goethite, epsomite and elemental sulfur produced by both hydroxylation and bacterial processes. The highest Tl contents were found in hydrothermal pyrite (200 mg kg^{-1}), kerogen (13 mg kg^{-1}), manganese ores (27 mg kg^{-1}) and iron sulfate-hydroxides (142 mg kg^{-1}). The aquatic kerogen was formed in a marine environment and later heavily carbonized during the hydrothermal processes. The Lodares outcrops exhibit interesting details on the geochemical cycle of Tl in a genetic frame of epithermal formation of pyrite and kerogen.

Keywords: Epithermal; Kerogen; Pyrite; Pyro-Bitumen; Thallium; Volcanogenic sulfide mineralization.

1. Introduction

The formation of iron oxide ore bodies in low-temperature hydrothermal systems has occurred in all geological periods frequently involving the formation of FeS_2 and FeAsS ores with Tl, Sb, Hg, Mn, Pb and Ba. During the hydrothermal formation and further weathering, these deposits are oxidized and the Fe hydrolyzed to form supergene iron and manganese ores, such as FeO(OH) (goethite) and $Fe(OH)_3$ (lepidocrocite) and pyrolusite (MnO_2) preserving variable amounts of the accessorial metals and metalloids. The complex hydrothermal origin of the iron-manganese ore bodies and the dual geochemical behavior of Tl, as lithophile and chalcophile element promoted recent worldwide studies on these topics [1–7]. The high toxicity of Tl and its presence in coals and carbonaceous sediments had prompted studies on its bioavailability and geochemical cycling in smelting ashes, soils, coals, etc. [8–14]. The Lodares (Soria, Spain) area deposits and other similar carbonate rock-hosted epithermal deposits could be interesting polymetallic sources, e.g., the Jas Roux deposit (France) with Tl phases hosted in Triassic calcareous rocks [15], the Alshar Au–As–Sb–Tl deposit (Macedonia) developed as a mineralized breccia at the contact of volcanic rocks with dolomites, jasperoid beds in the carbonate rocks, and vein–disseminated zones in dolomites and Tertiary volcanic rocks [16], or the case of Agdarreh (Iran) [17] which includes: (1) pre-ore decalcification with dolomite dissolution re-precipitation, (2) a first-stage silicification process associated with pyrite, (3) a second-stage silicification linked with precipitation of galena and, Hg-Tl-Sb-As sulfides, (4) late-stages of cinnabar and baryte in pockets; (5) oxide ore stage and carbonate alteration, e.g., complex Mn–Fe-rich oxy-hydroxides, arsenates, sulfates in residual leached rock and infill of karstic cavities. A possible explanation for the frequent Fe and Mn coupling and redox sensitive elements could be its hydrothermal origin associated to cap carbonates [18]. The geochemistry of shallow epithermal ores usually includes different proportions of Au, Ag, Te, Se, Hg, As, Sb and Tl pointing to geochemical cycles linked by their similar volatile behavior through subduction, partial melting in the mantle and late magma degassing processes [19,20]. The important epithermal Tl deposit of Xiangquan (China) is also hosted in micritic limestone and the ore is also composed by Tl-bearing pyrite including a low temperature association of Tl with As, Sb, Hg, Pb, Zn and Au [21]. Notwithstanding its toxicity and rarity, thallium is an important element employed in superconductive materials [22], medicine [23,24], electronics [25,26], chemical industries [27,28] and radiation dosimetry [29,30]. Accordingly, Tl is increasingly analyzed in varied environmental scenarios [31-34]. The Lodares outcrop exhibits organic kerogen deposited in the pyrite-dolomite pockets associated with recent sulfur-bacterial traces. The existence of pyro-bitumen inter-grown with polymetallic sulfides and baryte in epithermal ore deposits has been explained by the rapid thermal maturation of sedimentary organic matter by hydrothermal fluids [35]. This type of hydrothermal petroleum provides energy and carbon sources for a subsurface microbial community metabolizing hydrothermal sulfur minerals. The combination of hot water, carbon compounds and transition metal sulfide minerals, e.g., pyrrhotite and pyrite, have potential to facilitate essential catalytic chemistry for Earth's earliest life [36-38]. The nowadays closed Lodares quarry (41°12'04.8"N, 2°23'59.8"W) was exploited ca. 15 years ago to extract dolostone aggregates for road pavements. The Lodares area hosts a fossilized intra-Miocene geothermal field placed along an inferred geological fault oriented approximately WNW-ESE on the basis of the geographical alignment of fossil thermal springs which were historically mined to extract goethite-lepidocrocite Fe ores along ca. 15 km, i.e., Blocona, Lodares, Jubera, Velilla and Avenales quarries (Figure 1). The Lodares quarry exposes a well preserved stockwork structure of pyrite-rich mineralized veins hosted in sedimentary dolostones; i.e., an excellent natural scenario for Tl studies to shed new light on the formation on respective deposits by characterization of the so far undescribed Lodares case. Other important gap in knowledge that needs to be filled is the Tl electronic speciation and its related mineralogical phases. Accordingly, we collected both iron-manganese ores and host samples from the aligned quarries to be analyzed by ESEM-EDS, EPMA, ICP-MS, XRD, XAS, Raman-PL and FTIR to enquire on the primary and secondary geochemical distribution of Tl.

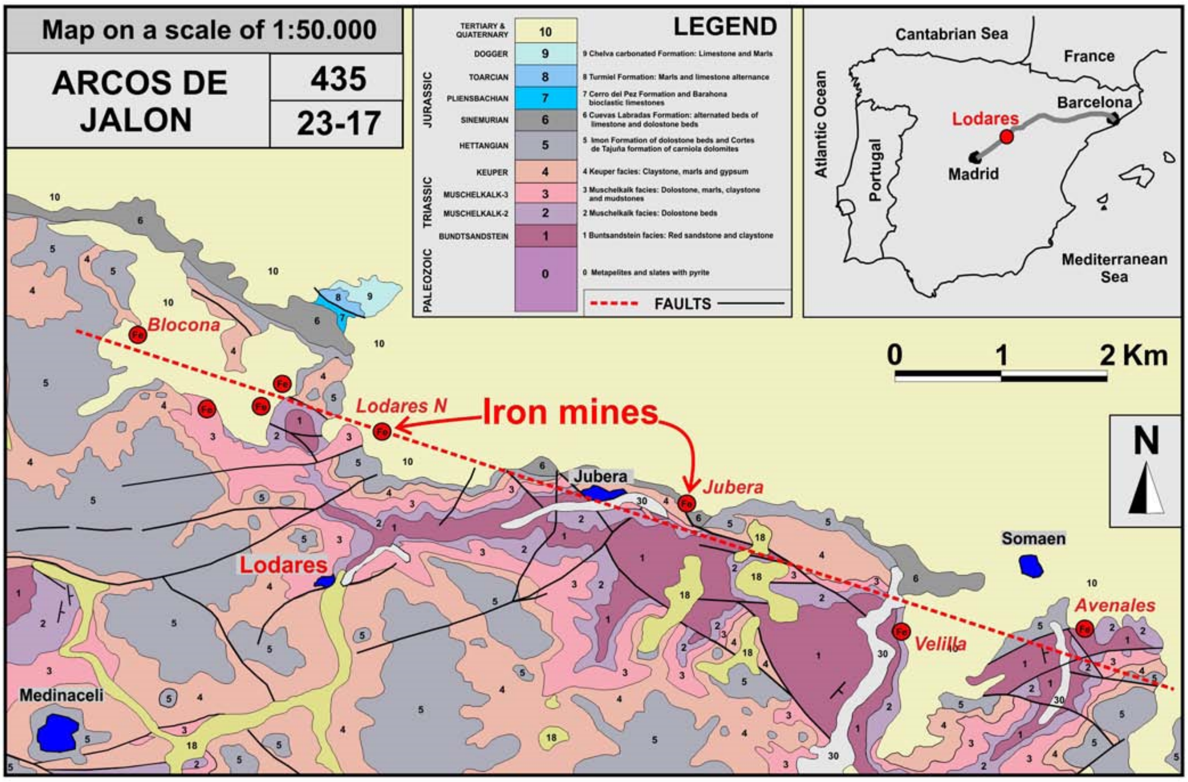

Figure 1.- Regional Geology of the studied area and location of iron-manganese mines

2. Geological frame of the Fe-Mn ore deposits

The iron-manganese ores are mainly goethite, lepidocrocite, pyrolusite and jarosite hosted in the whole stratigraphical column up to the Miocene and Pliocene carbonated conglomerates. The obvious WNW–ESE alignment of the Fe-Mn ore outcrops must be associated with a hidden deep fault in Paleozoic formations, i.e., a WNW–ESE striking fault with a right-lateral tectonics developed during Late Paleozoic and Early Triassic events and reactivated during the Late Jurassic to Early Cretaceous main rifting stage. During the Tertiary period up to present day, the deformation of this fault operates as right-lateral with slightly transpressive elements forming a 120 km long and 15 km wide overstep area [39] (**Figure 1**). The main studied quarry in Lodares (Soria, Spain) was open in a carbonated dolostone sequence of horizontal strata. It is a carbonated formation of the Triassic facies placed concordantly on the underneath Buntsandstein red sandstone strata which was only observed in the quarry through core borehole remains. This carbonated sequence is regionally placed in the upper dolomitic section of the Muschelkalk [40,41]. The front of the Lodares quarry exhibits both regional main features of the Muschelkalk facies, i.e., a lower section of stratified dolostones, and an upper section of grey and green marls with interspersed slab-shaped dolostone strata (**Figure 2**).

The bottom of the stratigraphical Muschelkalk sequence in Lodares is formed by mudstone beds with intermixed dolomitic layers and ripple mark structures. Subsequently above dolostone beds with ripple marks and cross stratification overlays. The column ends with more dolostone beds exhibiting hummocky and swale cross-stratification [42,43] and bioturbation in the upper section. During the deposition of the Muschelkalk dolostone unit the tidal plain included intertidal episodes with development of algal tapestries.

From the paleo-geographical point of view, the studied zone represents the margin between the Muschelkalk marine basin, with terrigenous facies, and the precipitation of carbonated facies deposited on a vast carbonated tidal plain. This type of dolomitic sediments suggests a fast transgression on the lower terrigenous materials of the Buntsandstein formation and a regressive sequence with more shallow-marine deposits and later the hyper-saline conditions of the overlying facies.

Preprints (www.preprints.org) | NOT PEER-REVIEWED | Posted: 17 January 2018 doi:10.20944/preprints201801.0155.v1

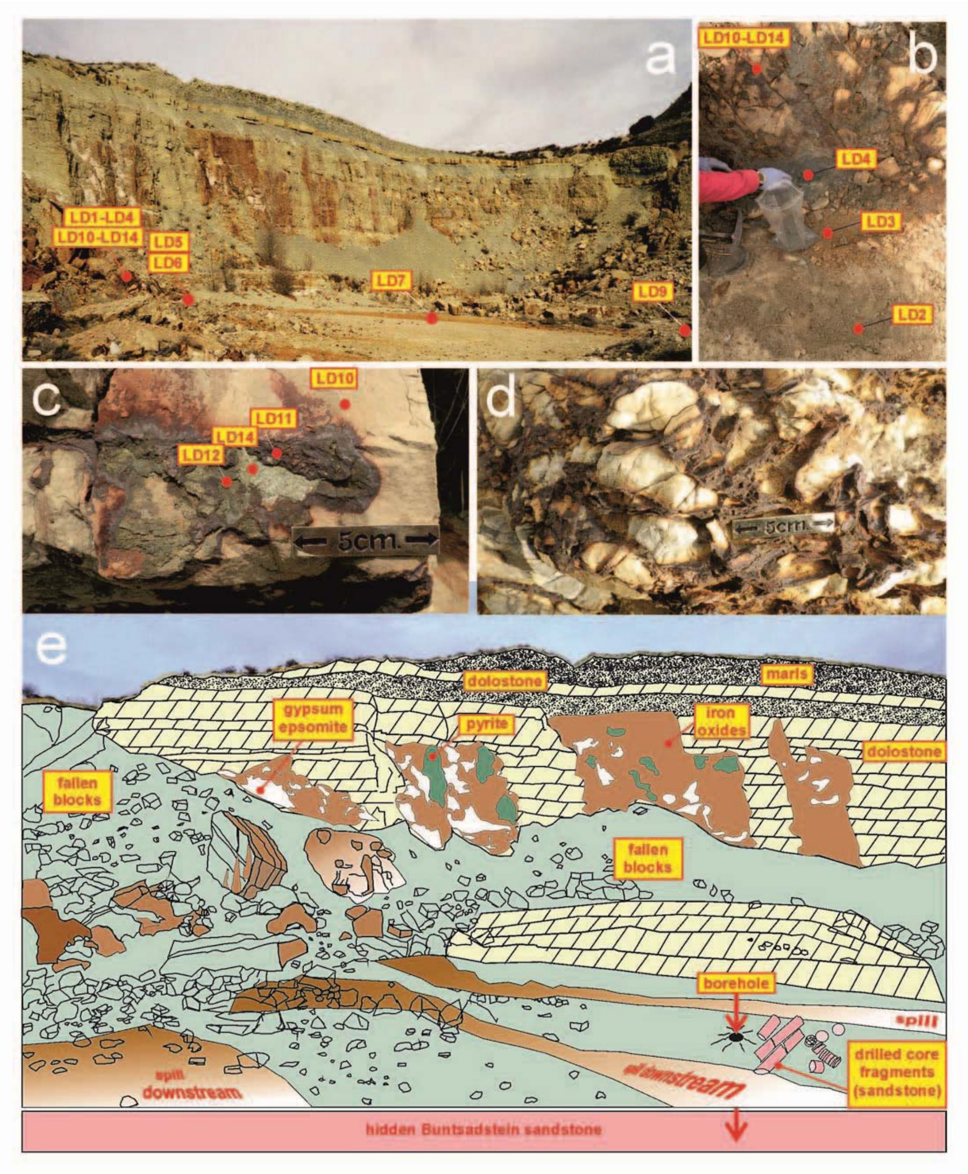

Figure 2.- Lodares quarry details (a) sampling and front of quarry, (b) collecting weathered pyrite, (c) and (d) details on pyrite, goethite and dolostone host rock, (e) labeling of different lithology and features. LD1 to LD14 refer to collected and analyzed samples.

3. Materials and Methods

3.1. Samples

Host rocks, kerogen, polymetallic ores and weathered hydrated phases were sampled from the Blocona, Lodares, Jubera, Velilla and Avenales quarries to be analyzed by ICP-MS, EPMA, ESEM-EDS, XRD, FTIR and Raman techniques (**Figure 3).**

All these iron-manganese ore quarries, mainly composed by goethite, lepidocrocite and pyrolusite are hosted in a NW–SE alignment depicted in Figure 1. The most detailed sampling was performed in the Lodares quarry (Figure 2) since it was worked recently, i.e., ca. 10 years ago, exhibiting relatively unaltered epithermal veins of pyrite, arsenopyrite, sphalerite dolomite, alkali feldspar, quartz, baryte and organic kerogen. Lodares offers unaltered polymetallic sulfides while other quarries only exhibit large volumes of Fe-Mn oxy-hydroxides and sulfated minerals mainly hosted in karstified tertiary limestones.

Samples labeled from LD1 to LD9 are weathered sediments mixed with altered dolostone host rock; LD10 is limestone host rock, LD11 is iron oxide covering, LD12 is disaggregated powdered pyrite of grey color, LD13 is salted efflorescence, LD14 is unaltered pyrite, LD15 is a polymetallic powdered mudstone of grey color and KERO is a kerogen collected in dolomite-pyrite vein pockets in the Lodares quarry. Concerning samples collected in other quarries, AVEN is Avenales; BLFE is goethite-lepidocrocite and BLMN pyrolusite from Blocona quarry, JUB is goethite-lepidocrocite from Jubera quarry and VEL is also goethite-lepidocrocite from the Velilla-Somaén open pit (Figure 3).

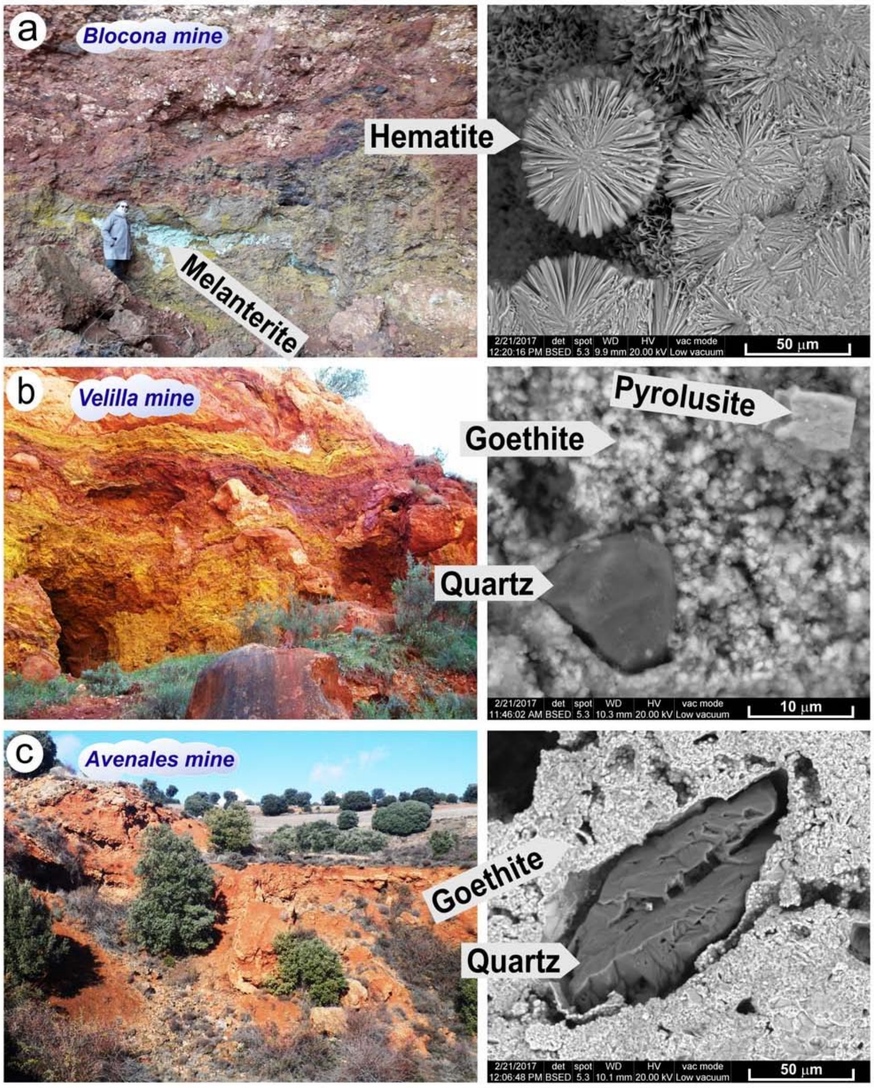

Figure 3.- Iron-manganese mines from Lodares area and associated minerals observed under the electron microscope: (a) Blocona (Hematite), (b) Velilla-Somaén (pyrolusite, goethite, quartz), (c) Avenales (goethite, quartz).

3.2. Environmental Scanning Electron Microscopy with Energy Dispersive Spectroscopy

Mineral crystal morphologies, textures, micro-structures, elements distribution, bacterial traces, corrosion pits and neo-formed phases were studied under an ESEM-EDS microscope (Philips FEI INSPECT Hillsboro, Oregon, USA), operating at low vacuum conditions to analyze the samples preserving their natural shapes and avoiding metallic coatings and dehydration processes. The ESEM resolution working at low-vacuum was at 3.0 nm/30 kV (SE), 4.0 nm/30 kV (BSE) and <12 nm/3 kV (SE). The accelerating voltage was at 200 V - 30 kV and the probe current up to continuously adjustable 2 μA. To achieve comparative analytical results, we operated in low-vacuum mode with a backscattered electron detector (BSED) under vacuum conditions of 30 Pa, a high voltage of 20 kV, an appropriate beam spot size for particular magnifications and to reach good focus and astigmatism correction and a working distance of approximately 12 mm to the detector. The EDS measurements were performed with an energy-dispersive X-ray spectrometer (INCA Energy 200 energy dispersive system, Oxford Instruments). The software used for the quantification was Microanalysis Suite, INCA suite version V.4.

3.3.- Electron Probe Micro-Analysis

The chemical features of Fe-oxide hydroxides and sulfides were determined on the basis of data series of EPMA analyses (Jeol Superprobe JXA-9800M), bulk and channel-selected (TAP, PETJ, LIF, PETH) X-ray spectra searches and identification routines. Galena (PbS) for S and pure metals for Ni, Fe, and Cu were used as standards from a collection stored at the Servicio de Microscopía Electrónica Luis Bru, Complutense University, Madrid. The accelerating voltage was 20 kV, the beam current 50 nA and the beam diameter 1 to 5 μm. For the Tl amount measurements, the EPMA equipment was calibrated using an international standard of a quartz vein sample from Lookout Pass, Tooele County, Utah, USA containing weissbergite ($TlSbS_2$), picotpaulite, ($TlFe_2S_3$) and pyrite (FeS_2).

3.4.- Inductively Coupled Plasma-Mass Spectroscopy

The ICP-MS analyses were performed after a four-acid digestion technique (sequential addition of hydrofluoric acid, hydrochloric acid, nitric acid and perchloric acid) and measurement by

Inductively Coupled Plasma-Optical Emission Spectroscopy (ICP-OES; Agilent, model: 725-ES) to identify major elements such as Na, Mg, Al, K, Ca, Fe and S elements and by Inductively Coupled Plasma-Mass Spectroscopy ICP-MS (Perkin Elmer, model: NexION 300D) for minor and trace elements such as Cd, V, Cr, Mn, Fe, Hf, Ni, Er, Be, Ho, Hg, Ag, Sr, Tl, Pb, U, Zr, Zn, Nb, Rb, La, Ta, Sb, Y, Mo and Cs. All ICP-MS analyses were performed by MS Analytical laboratory (Langley, British Columbia, Canada). In all cases duplicate samples were analyzed with appropriate standards and blanks. Finally, corrections were made for the spectral inter-element interferences.

3.5.- X-Ray Diffraction analysis

Mineral identification and semi-quantification were performed by XRD analysis of the powdered samples on a Philips PW-1710/00 diffractometer using the CuKα radiation with a Ni filter and a setting of 40 kV and 40mA. The used XPowder software (J.D.Martin-Ramos, Univ. Granada, Spain) permits also a full duplex control of the apparatus. The qualitative analyses were based on the ICDD-PDF2 and DIFDATA databases. We utilize Boolean searching and chemical restraints to the initial abundant elements (S-Fe-Mn-Mg-Ca) in the limestone Fe-Mn quarries. Additional calculations on the unit-cell refinement, space group, systematic *hkl* extinctions, $K_{\alpha2}$ stripping, Fourier and functional filtering, FWHM and integrated width parameters could be calculated with the XPowder software.

3.6.- Micro-Raman and Photoluminescence analysis

The Micro-Raman spectra of polymetallic samples and associated hydrated weathered phases were recorded in a Thermo-Fischer DXR Raman-PL microscope. The system has a point-and-shoot Raman ability spot of 1 µm spatial resolution. We used the 100× objective of the confocal microscope together with a 532 nm laser source delivering 10 mW at 100 % of the laser power mode. The average spectral resolution in the Raman shift ranging from 100 to 4000 cm^{-1} was 4 cm^{-1}, with 900 lines/mm grating and 2 µm spot size in our measurements. The system was operated under OMNIC 1.0 software fitting working conditions such as pinhole aperture of 25 µm, bleaching time 30 s; average of four exposures timed 10 s each.

3.7- XANES spectroscopy

Powdered samples were analyzed by Tl L_{III}-edge XANES spectroscopy at the Synchrotron Radiation Source at the Karlsruhe Institute of Technology (Karlsruhe, Germany). The powdered kerogen sample was pressed into a 13-mm pellet and was analyzed at the SUL beamline, the powdered samples LD1, LD3, LD4 and LD5 were prepared in powder sample holders and analyzed at the XAS beamline. All spectra were collected at room temperature in fluorescence mode, using a

7-element Si(Li) solid state detector at the SUL beamline and a 5-element silicon drift detector at the XAS beamline. To attenuate the very intense As Kα fluorescence line that interfered with the detection of the Tl Lα fluorescence line, a Ga-filter (6 absorption lengths) was placed in front of the fluorescence detectors (which, however, resulted in a much smaller but still disturbing background signal form the Ga Kβ fluorescence line). The reference spectra of Tl_2O_3 (avicennite), Tl(I)-illite (Tl^+ adsorbed onto illite), and $TlAsS_2$ (lorandite) were available from previous work [45]. The spectrum of Tl(I)-jarosite from Dutrizac et al. (2005) [46] was kindly provided by Suzanne Beauchemin (Natural Resources Canada). For data extraction, the software code Athena was used [47]. Owing to the high noise level in the sample spectra, data interpretation was limited to visual comparison of sample with reference spectra.

3.8.- Fourier Transform Infrared Spectroscopy in attenuated total reflection mode

The FTIR-ATR spectroscopy analyses of pulverized kerogen samples collected in the Lodares quarry were obtained on an Agilent Cary 630 FTIR spectrophotometer using an Agilent diamond attenuated total reflectance (ATR) accessory to avoid the characteristic water absorbance with the KBr pellets producing undesirable overlapping in important spectral regions such as 3400 and 1620 cm^{-1}. The spectral acquisition range was 4000 to 400 cm^{-1}. Measurements of the intensity of different bands corresponding to the major functional groups of the molecule were performed to facilitate the pattern recognition from the spectra; a mathematical procedure was applied to increase its resolution, based on the digital subtraction of the original spectrum of a positive multiple of its 2nd derivative [44].

4. Results

4.1.- Ore deposits of iron-manganese minerals

The initial field exploration allowed the detection of epithermal chimneys along the working zone between Medinaceli and Arcos de Jalón (ca. 15 km) and their relationships with the Triassic, Jurassic and Tertiary facies (**Figure** 1). No Paleozoic metapelite outcrops were found but they are deeply buried underneath and exposed in the surroundings exhibiting hydrothermal veins of quartz with polymetallic sulfide phases. The location of the Fe-Mn quarries are roughly aligned and oriented ca. WNW–ESE which could be associated with a buried deep fault occurring in the Paleozoic metapelites rocks (**Figure** 1). This observation agrees with a right-lateral tectonics developed initially through Late Paleozoic and Early Triassic events. Furthermore, the Fe-Mn epithermal ores are hosted in the Tertiary karstified limestones, i.e., Avenales, Velilla, Jubera and Blocona quarries (**Figure** 3).

The fossilized epithermal chimneys of the Lodares area contain unaltered minerals coming from lower stratigraphic levels dragged upwards by ascending hydrothermal fluids, as follows: (1) quartz and feldspar grains from the Buntsandstein sandstone together with probable iron reduced to pyrite by the epithermal SO_2 gases, (2) dolostone rock fragments with narrow beds of black color with apparent relationships with former algae tapestries after the hydro-pyrolysis processes, (3) neo-formed kerogen deposited in pockets together with dolomite and pyrite among other accessorial epithermal phases, i.e., sphalerite, cinnabar, stibnite, thallium-bearing pyrite, etc. However, the other quarries, viz., Blocona, Jubera, Velilla and Avenales minerals are more altered showing large masses of Fe-Mn oxy-hydroxides and sulfates, but not sulfide and sulfosalt minerals (**Figure**s 2, 3).

Table 1 and **Figure** 3 display ESEM photomicrographs and EDS elemental analyses of samples collected in the Fe-Mn quarries to perform an initial approach to the study of accessorial Tl in the hydrothermal mineralization phases. The Fe-Mn masses exhibited minor differences among them, as follows: (i) Blocona quarry exhibit the greatest volume of manganese ores, mainly pyrolusite, as determined by XRD, and Fe hydrated sulfates, mainly melanterite and rozenite by XRD, together with important amounts of hematite-goethite fibrous masses (**Figure** 3a). (ii) Velilla-Somaen quarry shows mixed masses of reddish FeO(OH) goethite and yellowish Fe(OH)3 lepidocrocite, also determined by XRD, together with variable amounts of quartz and pyrolusite (**Figure** 3b). (iii) Avenales shows more homogeneous goethite masses with corroded quartz grains (**Figure** 3c).

Table 1.- ESEM-EDS analyses of the Fe-Mn epithermal mineralizations

	Avenales quarry				Blocona quarry						Jubera quarry			Velilla-Somaén quarry					
Element	Aven1 (%)	Aven2 (%)	Aven3 (%)	Aven4 (%)	BloFe1 (%)	BloFe1 (%)	BloFe2 (%)	BloMn1 (%)	BloMn2 (%)	BloMn3 (%)	Jub1 (%)	Jub2 (%)	Jub3 (%)	Vel1 (%)	Vel2 (%)	Vel3 (%)	Vel4 (%)	Vel5 (%)	Vel6 (%)
C K	1.05	2.30	0.00	0.00	5.09	5.09	0.00	4.23	0.00	0.00	0.00	0.00	0.00	9.16	0.00	0.00	0.00	2.33	10.74
S K	0.00	0.00	0.00	0.00	0.00	0.00	0.00	0.00	0.00	0.00	0.00	0.00	0.00	0.50	0.00	0.00	0.21	0.54	0.00
P K	0.00	0.00	0.00	0.00	0.00	0.00	0.00	0.00	0.00	0.00	0.00	0.00	0.26	0.43	0.00	0.00	0.00	0.00	0.00
Ca K	0.49	0.29	0.24	0.00	0.25	0.25	0.00	0.00	0.78	0.32	0.88	0.00	0.39	0.73	0.46	0.27	0.68	0.47	0.00
Na K	0.00	0.00	0.00	0.00	0.00	0.00	0.20	0.42	0.32	0.30	0.55	0.00	0.00	0.00	0.36	0.26	0.00	0.00	0.00
K K	0.00	0.00	0.00	0.00	0.00	0.00	0.00	0.00	2.19	0.52	0.36	0.00	0.00	0.81	0.20	0.26	0.55	1.12	0.00
Al K	0.62	0.24	0.36	0.00	0.29	0.29	0.00	0.00	0.31	0.45	0.37	0.00	0.77	1.60	0.82	0.73	1.94	3.18	0.42
Si K	0.97	2.34	0.56	36.90	1.10	1.10	36.42	0.19	0.18	0.55	0.62	66.16	1.23	3.17	1.47	33.43	4.09	5.49	0.73
Fe K	65.98	56.24	45.58	19.07	42.86	42.86	0.99	0.84	0.80	1.51	20.70	4.45	56.13	41.86	9.30	7.26	47.3	14.11	5.47
Mn K	0.00	0.00	0.00	0.00	0.00	0.00	0.00	42.28	50.39	58.34	32.54	2.92	2.65	0.00	45.93	0.00	0.31	0.00	0.75
Ba L	0.00	0.00	0.00	0.00	0.00	0.00	0.00	0.00	7.49	1.68	2.09	0.00	0.00	0.00	0.00	0.00	0.00	0.00	0.00
Mg K	0.00	0.28	0.00	0.00	0.43	0.43	0.00	0.00	0.31	0.40	0.86	0.00	0.40	0.39	0.00	0.12	0.62	0.64	0.00
Ti K	0.00	0.00	0.00	0.00	0.21	0.21	0.00	0.00	0.00	0.00	0.00	0.00	0.00	0.00	0.00	0.00	0.00	0.00	0.00
Hg M	0.00	0.00	0.00	0.00	0.00	0.00	0.98	0.00	0.00	0.00	0.00	0.00	0.00	0.00	0.00	0.00	0.00	0.00	0.00
Ag L	0.00	0.00	23.70	0.00	0.00	0.00	0.00	0.00	0.00	0.00	0.00	0.00	0.00	0.00	0.00	0.00	0.00	0.00	0.00
Pb M	0.00	0.00	0.00	0.00	0.00	0.00	0.00	0.00	0.00	0.00	0.00	0.00	0.00	0.00	0.00	0.00	0.00	31.22	62.26
Tl M	0.00	0.00	0.00	0.00	0.00	0.00	0.54	0.00	0.00	0.00	0.00	0.00	0.00	0.00	0.00	0.86	0.00	0.00	0.00
As L	0.60	0.00	0.00	0.00	0.00	0.00	0.00	0.00	0.00	0.00	0.00	0.00	0.00	0.00	0.00	0.00	0.00	0.00	0.00
O	30.29	38.31	29.56	44.03	49.76	49.76	60.87	52.04	37.23	35.93	41.03	26.47	38.17	41.35	41.46	56.80	44.30	40.90	19.63
Totals	100.00	100.00	100.00	100.00	100.00	100.00	100.00	100.00	100.00	100.00	100.00	100.00	100.00	100.00	100.00	100.00	100.00	100.00	100.00

This general overview of the Fe-Mn quarries demonstrates a general high hydration grade which implies Tl leaching in the Fe-Mn masses (Table 1). Unaltered pyrite specimens contain more Tl by ICP-MS compared with those other more altered pyrite samples. This Table 1 only shows well known geochemical affinities in Fe-Mn ores, such as Ba-Mn, host rock contamination (C, Ca, Mg), inherited grains of quartz and feldspar from the buried Buntsandstein sandstones (Si, Al, K, Na), and the main mineralization (Fe, Mn) and epithermal polymetallic residual phases (Ag, Pb, Hg) hosted in the Fe-Mn ores. An interesting feature in quartz grains inlaid in Blocona goethite masses was observed in the initial ESEM-EDS analyses (Table 1).

Two different types of quartz grains were observed: one preserving up to 850 mg kg^{-1} of Tl, as measured by EDS, in spite of the general hydrothermal alteration processes and later weathering, and other type, lacking of Tl. Further ESEM-EDS analyses focused on quartz grains of the Blocona Fe-Mn mineralization (**Figure** 4) were performed to compare micro-morphological characteristics of both type of quartz grains, i.e., with and without Tl.

	Blocona Mine:	*Fresh Quartz*							*Corroded Quartz*		
Element	**Bloc1** (%)	**Bloc2** (%)	**Bloc3** (%)	**Bloc4** (%)	**Bloc5** (%)	**Bloc6** (%)	**Bloc9** (%)	**Bloc10** (%)	**Bloc7** (%)	**Bloc8** (%)	**Bloc11** (%)
S K	0.00	0.00	0.00	0.00	0.00	0.00	0.00	0.00	0.30	0.45	0.43
Ca K	0.00	0.00	0.00	0.00	0.00	0.00	0.00	0.00	0.34	0.25	0.20
C K	0.00	0.00	0.00	0.00	0.00	1.68	0.00	0.00	2.11	0.00	0.00
Na K	0.00	0.00	0.00	0.00	0.00	0.25	0.25	0.00	0.00	0.30	0.27
Al K	0.28	0.23	0.00	0.00	0.35	0.36	0.31	0.00	0.00	0.32	0.30
Si K	42.10	41.33	44.34	43.55	42.30	38.80	41.33	43.01	36.92	43.24	42.59
Fe K	5.65	6.10	2.08	3.23	4.27	5.30	5.96	4.19	8.43	1.88	3.27
Hg M	0.80	1.61	1.16	1.28	2.14	1.27	1.39	1.16	0.00	2.15	1.80
Tl M	0.46	0.77	0.88	0.81	0.60	0.85	0.61	0.71	0.00	0.00	0.00
O	50.71	49.95	51.54	51.14	50.34	51.49	50.15	50.92	51.89	51.41	51.15
Totals	100.00	100.00	100.00	100.00	100.00	100.00	100.00	100.00	100.00	100.00	100.00

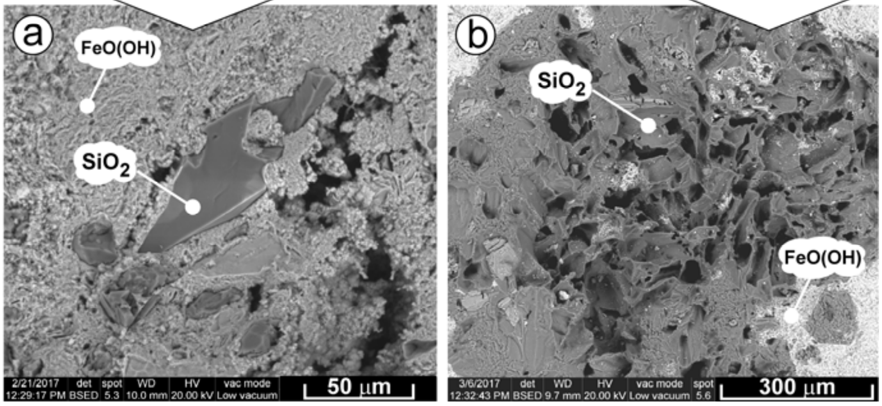

Figure 4.- ESEM-EDS analyses and photomicrographs of unaltered and altered quartz grains from Blocona mine (BLOC). Note differences among thallium EDS analyses.

Figure 4a exhibits a representative unaltered quartz grain inlaid in goethite together with eight EDS chemical-elemental analyses of these quartz types exhibiting different proportion of Tl from 0.46% up to 0.85%. Conversely, **Figure** 4b displays an ESEM picture of a representative quartz grain with corrosion pits together in which Tl was not detected in three EDS analyses. It is difficult to explain the high Tl and Hg contents in some quartz clusters, since both Tl and Hg are unlikely to fit into the crystal structure of quartz; accordingly, we speculate that Tl and Hg are contained in an admixed nanoparticulate mineral phase below the resolution limits of our EPMA and ESEM electron microscopes. Additional experiments are planned to further resolve the Tl- and Hg-bearing phases associated with quartz.

4.2.- Weathered hydrothermal pyrite-kerogen-thallium parageneses

Conversely to other Fe-Mn outcrops previously described, the Lodares quarry has been operative till very recently exhibiting a relatively unaltered iron-sulfides mineralization including Tl, Hg and Sb together with kerogen pyro-bitumen and hydrated secondary minerals. Accordingly, we collected additional samples in this new outcrop to study host rock, primary (hydrothermal) and weathered phases using complementary analytical techniques.

Table 2.- Mineralogical analyses of the main phase collected in the Lodares quarry performed by X-ray diffraction (powder method)

Table 2

	LD1 (%)	LD2 (%)	LD3 (%)	LD4 (%)	LD5 (%)	LD6 (%)	LD7 (%)	LD8 (%)	LD9 (%)	LD10 (%)	LD11 (%)	LD12 (%)	LD13 (%)	LD14 (%)	LD15 (%)	BLMn (%)	BLFe (%)	JUB (%)	VEL (%)	AVEN (%)
Gypsum	40	4	65	66	70	1	--	--	--	--	28	51	3	8	--	--	--	--	--	--
Pyrite	30	--	--	22	18	--	--	--	--	--	--	21	--	77	--	--	--	--	--	--
Sphalerite	15	--	--	3	6	--	--	--	--	--	1	3	--	15	--	--	--	--	--	--
Quartz	4	4	2	2	3	1	4	2	8	--	--	2	1	--	2	--	--	--	--	--
K-Feldspar	5	2	--	--	--	--	4	--	6	--	--	--	--	--	--	--	--	--	--	--
Jarosite	6	--	33	--	--	--	--	--	--	--	21	--	--	--	--	--	--	--	--	--
Dolomite	--	90	--	--	--	97	90	90	69	100	44	--	4	--	--	--	--	--	--	--
Anhydrite	--	--	--	3	--	--	--	--	--	--	--	--	--	--	--	--	--	--	--	--
Barite	--	--	--	4	--	--	--	--	--	--	--	4	--	--	--	--	--	--	--	--
Scorodite	--	--	--	--	3	--	--	--	--	--	--	16	7	--	--	--	--	--	--	--
Moscovite	--	--	--	--	--	1	--	--	--	--	--	--	--	--	--	--	--	--	--	--
Calcite	--	--	--	--	--	--	2	8	15	--	--	--	--	--	98	--	--	--	--	--
Anglesite	--	--	--	--	--	--	--	--	2	--	--	--	--	--	--	--	--	--	--	--
Goethite	--	--	--	--	--	--	--	--	--	--	6	--	--	--	--	--	62	66	68	52
Hematite	--	--	--	--	--	--	--	--	--	--	--	--	--	--	--	--	26	28	27	41
Elem. sulfur	--	--	--	--	--	--	--	--	--	--	--	3	--	--	--	--	--	--	--	--
Epsomite	--	--	--	--	--	--	--	--	--	--	--	--	65	--	--	--	--	--	--	--
Hexahydrite	--	--	--	--	--	--	--	--	--	--	--	--	20	--	--	--	--	--	--	--
Pyrolusite	--	--	--	--	--	--	--	--	--	--	--	--	--	--	--	96	--	--	--	--
Amorphous	--	--	--	--	--	--	--	--	--	--	--	--	--	--	--	4	7	5	6	7
TOTALS	100	100	100	100	100	100	100	100	100	100	100	100	100	100	100	100	100	100	100	100

LD1..LD15 are Lodares samples, BLMn Blocona pyrolusite, BLFe Blocona goethite, JUB, VEL and AVEN are Jubera, Velilla and Avenales goethite samples

Both Figure 3 (outcrop) and Figure 5 (ESEM photos) display views of neo-formed hydrated sulfated minerals of white and pale colors such as gypsum, epsomite or jarosite. ESEM microscope observations of these samples shows: (1) newly-formed crystals of dolomite (Figures 5a&b); (2) hydrothermal baryte and neo-formed gypsum (Figures 5a&f); (3) hydrothermal pyrite with bacterial traces similar to those observed in experimental cultures of Acidithiobacillus ferrooxidans [48] and secondary scorodite (Figures 5a,e&d) and (4) kerogen masses filling in fissures in neo-formed pyrite and dolomite (Figures 5a&c). Table 2 summarizes semi-quantitative XRD analyses of fifteen samples collected in various parts of the Lodares quarry (Figure 2).

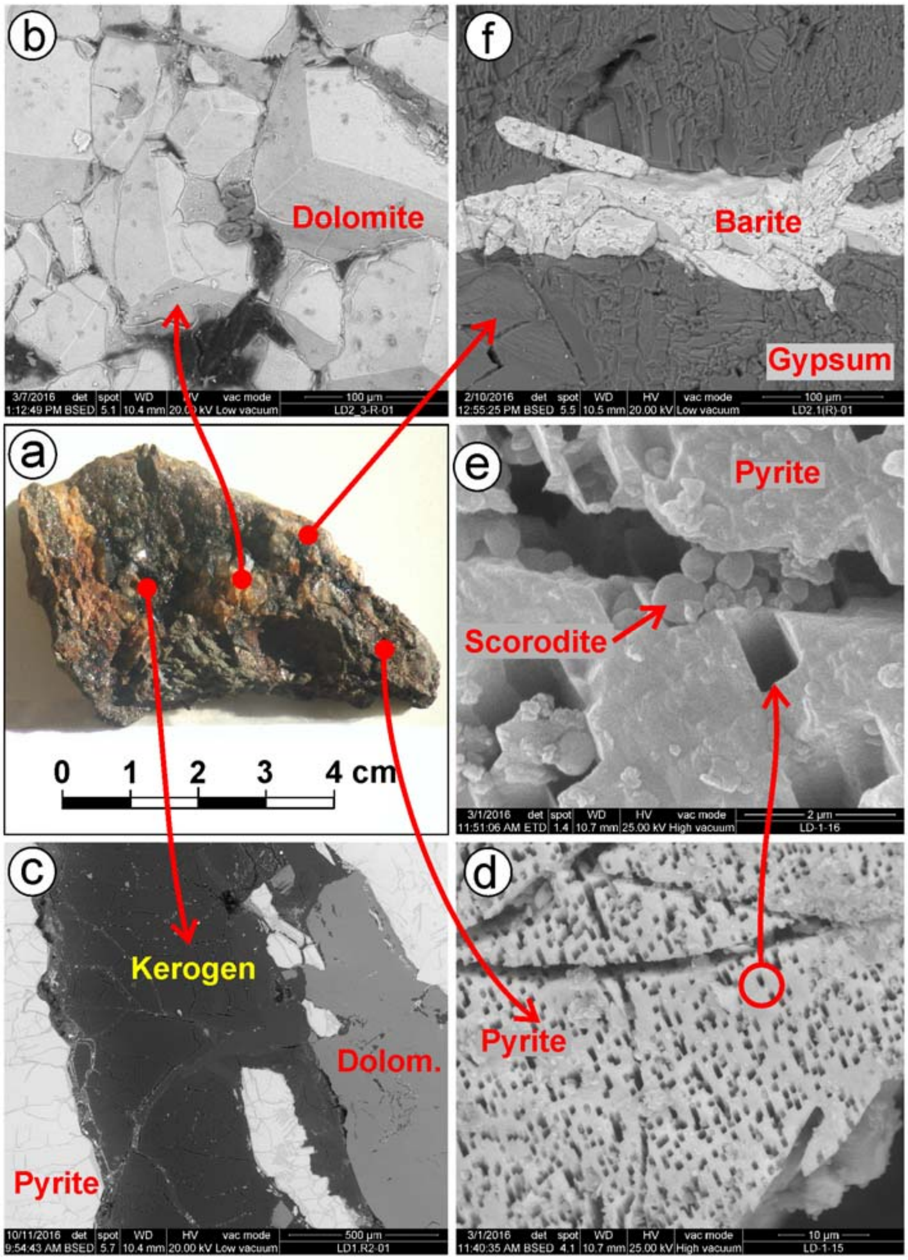

Figure 5.- Lodares hydrothermal rock, mainly composed by dolomite, pyrite and kerogen, under the ESEM microscope: (a) hand specimen, (b) dolomite rhombohedral crystals, (c) kerogen, (d) pyrite crystal exhibiting characteristic bacterial corrosion pits, (e) scorodite in fissures and corrosion pits of pyrite crystal,(f) hydrothermal baryte hosted in gypsum masses.

Taking into account that Tl is primarily held in pyrite; the sediments included in the brown spill downstream contain decreasing Tl concentrations with distance from the sulfide sources (**Figure** 2). We analyzed more Tl amounts, by ESEM, EPMA and IC`P-MS techniques, in unaltered pyrite masses compared to the weathered pyrite masses which always show minor Tl contents. Other characteristic paragenetic Tl bearing elements such as Sb, Hg and As display similar behavior.

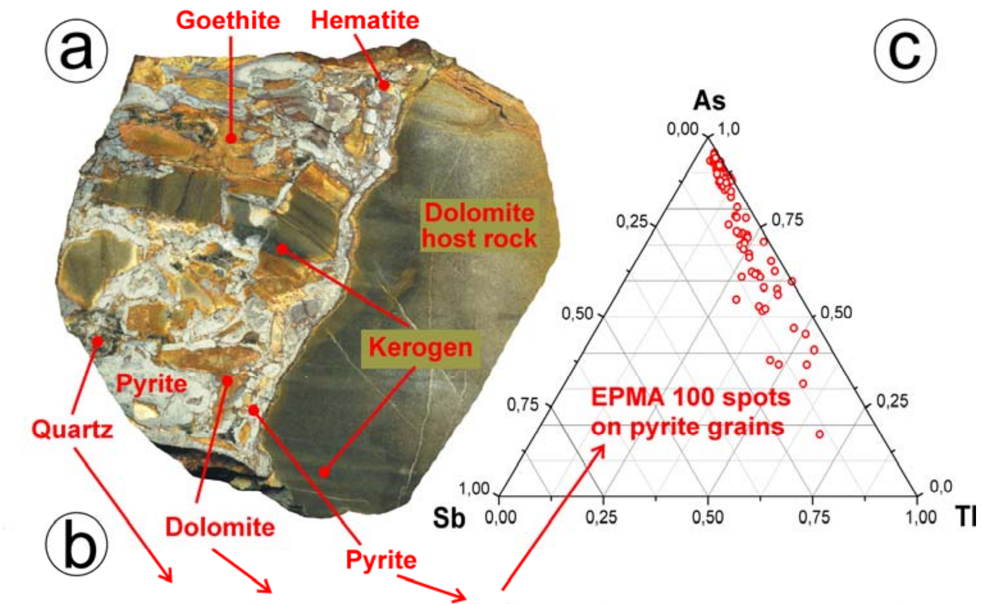

	Quartz	Dolom	Scorod	Pyrite	K-Feld	Goeth	Hemat	Barite
Elem.	(%) wt	(%) wt	(%) wt	(%) wt	(%) wt	(%) wt	(%) wt	(%) wt
O	55.11	45.95	27.46	0.00	46.83	42.73	33.99	25.52
Tl	0.01	0.02	0	0.10	0.09	0.00	0.02	0.11
S	0.01	0.01	2.74	53.58	0.01	8.47	1.91	14.42
Mn	0.01	0.03	0.01	0.00	0.01	0.01	0.03	0.02
Na	0.00	0.02	0.04	0.00	0.63	0.09	0.01	0.14
As	0.00	0.00	25.3	0.12	0.00	1.11	2.98	0.02
Hg	0.00	0.06	0.00	0.00	0.00	0.00	0.00	0.00
Pb	0.00	0.00	0.04	0.15	0.01	0.02	0.03	0.07
Fe	0.39	0.26	25.75	45.84	0.07	42.03	49.97	1.34
Al	0.00	0.13	0.06	0.02	10.03	1.47	1.57	0.31
Si	44.08	0.07	0.47	0.00	31.01	1.67	2.24	0.00
Ba	0.03	0.00	0.04	0.00	0.03	0.00	0.03	57.17
K	0.01	0.11	0.04	0.00	10.17	0.61	0.74	0.00
Mg	0.00	14.53	0.079	0.02	0.00	0.65	0.94	0.03
Sb	0.02	0.09	0.05	0.02	0.65	0.05	0.07	0.02
Zn	0.00	0.02	0.00	0.02	0.07	0.06	0.10	0.01
Ca	0.01	26.34	0.017	0.01	0.09	0.14	0.34	0.03
Total	**99.68**	**87.64**	**82.10**	**99.88**	**99.70**	**99.11**	**94.97**	**99.21**

Figure 6.- Lodares hydrothermal rock under the EPMA microscope: (a) polished hand specimen (b) EPMA spot average analyses of the observed phases (c) Ternary As-Sb-Tl compositions of one hundred EPMA spot analyses performed on pyrite grains.

3.3.- EPMA and ICP-MS analyses of thallium-bearing samples

The mining activities in the Lodares quarry resulted in the environmental exposure of epithermal veins of pyrite, arsenopyrite, sphalerite dolomite, alkali feldspar, quartz, baryte and organic kerogen.

To gain further insight into the Tl mineralization and the release of Tl from weathering hydrothermal outcrops, the elemental composition of twenty-one samples of thallium-bearing pyrite ores and related weathering products was determined using ICP-MS (Table 3 and Figure 7). In addition, the mineral distribution and element associations of Tl were examined by EPMA (Figure 6). We analyze such mineral paraganeses including both primary and secondary phases, by EPMA to perform chemical analyses of mineral phases, but mainly, to determine Tl element in more than 100 spots of unaltered pyrite grains (**Figure** 6).

We plotted the EPMA chemical data for As, Sb and Tl elements as a ternary diagram (Figure 6) to observe geochemical affinities among Hg-Tl-Sb epithermal elements and their hydrothermal origin associated to pyrite masses, which frequently contain 200 mg kg-1 Tl. ICP-MS analyses returns lower Tl and Hg concentrations than local analyses by SEM-EDX or EPMA. It is clear that Tl and Hg may be concentrated in localized mineral phases

Table 3.- ICP-MS analyses of the iron-manganese samples and associated parageneses.

			Labels for samples from the different quarries refer to t he Material and Methods section																				
	Unit Sym	**Detec Limit**	**LD1**	**LD2**	**LD3**	**LD4**	**LD5**	**LD6**	**LD7**	**LD8**	**LD9**	**LD10**	**LD11**	**LD12**	**LD13**	**LD14**	**LD15**	**KERO**	**BLFE**	**BLMN**	**JUB**	**VEL**	**AVEN**
Fe	%	0.01	27.8	5.51	14.9	22.7	20.6	6.46	3.49	2.71	2.22	0.64	23.5	19.4	5.49	34.4	0.60	1000	35.00	31.00	22.00	21.00	37.00
Al	%	0.01	0.19	2.54	1.31	0.28	0.22	2.66	2.06	1.68	2.18	1.00	1.00	0.15	1.00	1.00	0.22	0.00	1.00	3.00	1.00	1.00	5.00
Na	%	0.01	0.00	0.03	0.02	1.00	1.00	0.04	0.03	0.03	0.04	0.01	0.01	0.00	0.00	0.00	4.00	138	2.00	43.00	3.00	2.00	2.00
Mg	%	0.01	0.12	564	0.36	6.00	11.0	583	718	648	637	102	119	1.00	511	0.02	0.65	0.00	12.00	3.00	9.00	9.00	18.00
K	%	0.01	0.13	1.19	0.71	0.24	0.17	1.42	0.94	1.07	1.17	0.03	0.02	0.11	0.01	0.01	0.57	0.00	6.00	11.00	12.00	3.70	7.30
Ca	%	0.01	1.98	9.60	5.38	2.69	3.41	92.9	11.7	13.1	12.4	17.7	6.50	3.47	0.88	0.32	22.8	10.0	43.83	10.76	71.18	54.9	68.75
Ag	ppm	0.01	4.42	1.88	1.39	4.42	3.80	1.66	1.18	0.78	0.60	0.25	0.69	5.04	1.24	0.81	0.44	14.40	314.0	1508	768.0	312.0	628.0
As	ppm	0.15	$>10^4$	3160	6100	$>10^4$	$>10^4$	2860	1180	835	602	35.50	$>10^4$	$>10^4$	2030	$>10^4$	149	2759	4383	107.6	7118	5487	6875
Cd	ppm	0.02	0.40	0.90	0.40	0.40	2.00	1.40	0.70	0.60	0.40	1.00	2.60	1.00	0.40	0.40	1.00	0.00	30.00	6673	54.00	23.0	76.00
Cr	ppm	1	10.5	21.5	17.8	12.1	11.6	21.7	17.7	13.8	20.1	4.20	4.00	5.90	5.90	8.40	4.70	690	13.00	1.00	2.00	2.00	5.00
Hg	ppb	0.01	15.1	250	660	16.5	22.2	70.0	20.0	20.0	10.0	10.0	180	10.7	40.0	21.4	20.0	0.00	48.90	0.01	50.00	50.00	50.00
Mn	ppm	5	39.0	429	82.0	25.0	49.0	459	837	562	516	817	471	37.0	143	19.0	4710	37.60	337.0	$>10^4$	871.0	477.0	1429
Mo	ppm	0.05	11.8	4.03	7.28	4.48	7.63	4.55	8.47	4.83	3.96	1.26	8.03	11.3	0.62	9.78	0.54	146.0	170.2	115.31	60.84	103.0	7687
Ni	ppm	0.2	16.2	26.1	16.0	17.0	15.7	28.9	26.1	20.7	21.7	2.60	76.6	33.7	17.4	21.7	21.8	320.0	68.70	51.35	22.60	11.40	60.70
Pb	ppm	0.5	311	133	120	59.8	147	127	207	126	93.3	10.0	59.6	196	3.10	129	4.40	449.0	3823	8.00	88.00	557.0	1094
Rb	ppm	0.1	4.80	32.4	22.6	7.00	4.90	33.6	25.5	26.2	29.2	0.40	0.70	3.30	2.00	2.00	5.20	98.00	99.00	14.00	9.00	36.00	125.0
Sb	ppm	0.5	41.1	8.70	18.2	12.5	70.7	8.00	7.40	3.80	3.00	0.40	34.4	61.8	2.30	70.7	0.90	26.00	72.00	6.00	70.00	102.0	191.0
Sr	ppm	0.2	54.2	134	82.6	53.1	14.4	132	126	98.3	110	35.1	26.2	31.1	2.50	2.60	170	8.24	232.0	141.56	301.0	284.0	292.0
Tl	ppm	0.02	126	20.7	55.0	77.2	130	22.9	6.59	3.49	3.34	0.23	61.1	102	0.23	188	3.01	13.20	7.00	24.60	142.0	9.00	273.0
U	ppm	0.1	0.80	3.20	1.60	0.60	1.10	3.50	5.80	3.90	3.60	2.50	4.70	1.20	0.60	0.20	0.30	161.0	25.00	148.00	19.00	17.00	26.00
V	ppm	1	4.00	43.0	24.0	3.00	5.00	46.0	46.0	32.0	38.0	7.00	9.00	4.00	2.00	1.00	16.0	3.15	77.00	1.00	423.0	204.0	293.0
Zn	ppm	0.1	194	504	565	487	897	655	350	294	209	25.0	3280	1480	161	331	9.90	78.60	488.0	309.00	206.0	203.0	422.0
Zr	ppm	0.5	10.0	37.0	27.0	30.0	35.0	36.0	29.0	22.0	27.0	1.00	17.0	32.0	3.00	29.0	5.00	48.00	167.0	83.00	45.00	79.00	147.0

Analytical Method: **IMS-230 Multi-Element, 0.2g, 4-Acid, ICP-AES/MS, Ultra Trace Level.** ***From:*** **MS Analytical Langley. British Columbia. Canada.**

Additional interesting data observed in Table 3 are the Pb concentrations in LD14, LD12 and LD11, i.e., 203, 98 and 61 mg kg-1 of Pb which demonstrates the presence of epithermal Pb in weathered samples which was also observed for Ag, e.g., LD12 sample, and Pb in the EDS analyses of the other Fe-Mn ores.

Similar behavior can be observed for Zn element showing LD14 with 300 mg kg^{-1} of Zn, LD12 with 1490 mg kg^{-1} of Zn and LD11 with 3 240 mg kg^{-1} of Zn. Conversely the group Hg-Sb-Tl reduces their proportions in sample when weathering increases (**Figure** 7). Finally, Figure 7 shows a representative plot of the geochemical behaviors of Hg, Tl and Sb in unaltered and weathered pyrite, goethite created from former pyrite masses and dolostone host rock.

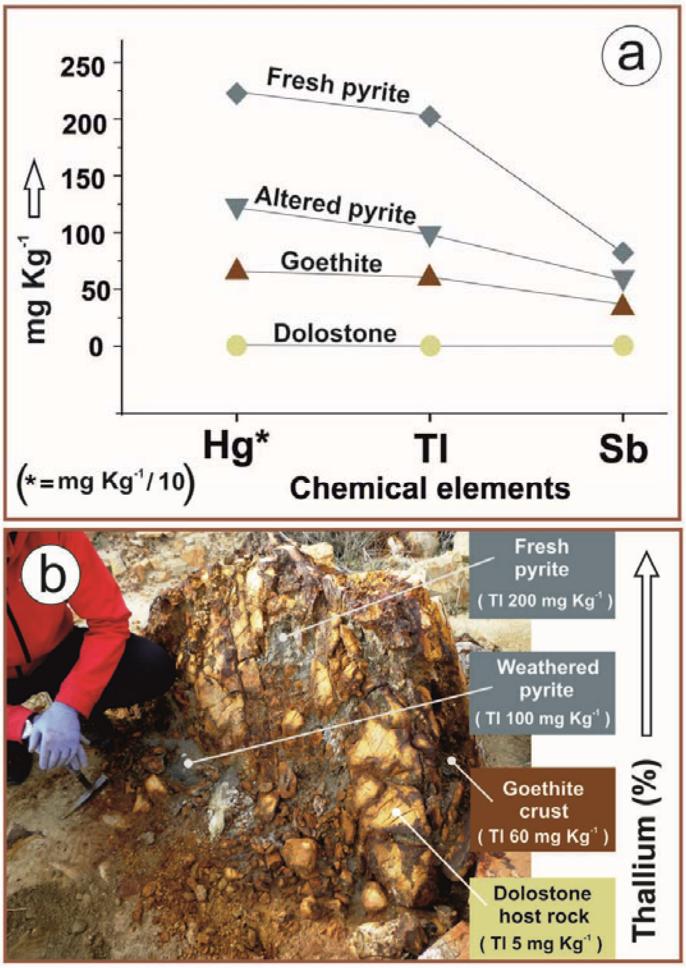

Figure 7.- ICP-MS analyses of samples from the Lodares quarry: (a) Variations in the chemical contents of Tl, Hg and Sb between unaltered pyrite, weathered pyrite, goethite-jarosite masses and dolostone host rock. (b) Note the clear differences among these materials and the strong corrosion textures.

4.4.- Tl L_{III}-edge XANES spectroscopy

In Figure 8, the Tl L_{III}-edge XANES spectra of the samples LD1, LD3, LD4, LD5 and the kerogen are compared to selected reference spectra: Tl_2O_3 and Tl(I)-jarosite are known secondary minerals from the weathering of Tl-containing metal sulfides, and Tl^+ adsorbed onto illite (or other micaceous clay minerals) has been identified as important pedogenic Tl species [45-47]. The spectrum of $TlAsS_2$ (lorandite) serves to represent Tl^I in metal sulfides in general. Owing to the very high As contents and the low Tl contents in the studied samples (Table 3), the quality of the sample spectra was limited. Nevertheless, comparison with the reference spectra suggested that neither Tl_2O_3 nor Tl(I)-illite were the dominant species in any of the studied samples. The spectra of the samples LD1 and kerogen exhibited a close similarity to the spectrum of TlAsS2, suggesting that Tl was predominantly associated with metal sulfides. The spectra of the samples LD3 and LD5, on the other hand, (relatively) closely matched the characteristic spectrum of Tl(I)-jarosite, suggesting that most Tl was contained in a mineral of the jarosite-dorallcharite series. The spectrum of the sample LD4 matched fairly to any of the references, suggesting that several Tl species contributed to the average Tl speciation

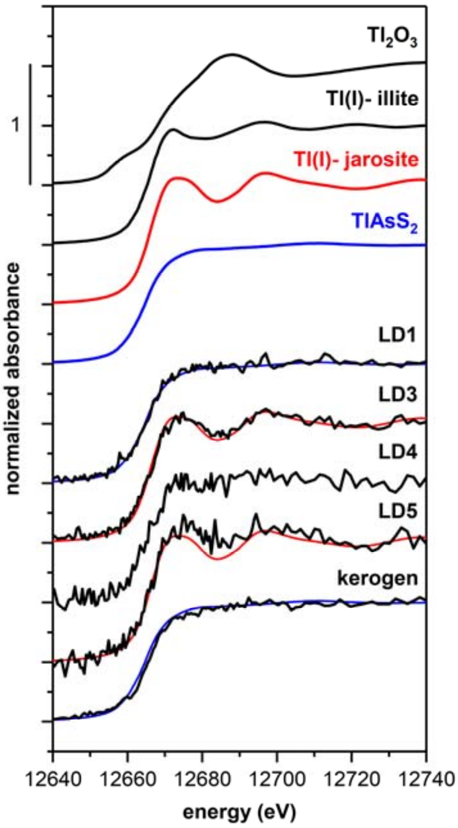

Figure 8.- Tl L_{III}-edge XANES spectra of samples LD1, LD3, LD4, LD5 and kerogen compared to reference spectra of Tl_2O_3 (avicennite), Tl(I)-illite, Tl(I)-jarosite (from ref. [46]) and $TlAsS_2$ (lorandite).

4.5.- Molecular characteristics of the hydrothermal kerogen

Figures 5a and 5c exhibit kerogen masses, as a hand-sample and a back-scattering image in the ESEM-EDS electron microscope. The available amount of sample was very scarce in the quarry front (**Figure** 2a) but enough to extract powder for FTIR and Raman-PL analyses and to prepare polished sections to be observed in the EPMA and ESEM microscopes. **Figure** 9a displays a representative Raman-PL spectrum of the Lodares kerogen with the characteristic peaks at ca. 1589 cm^{-1} (G-band) and 1358 cm^{-1} (D-Band) of carbon materials.

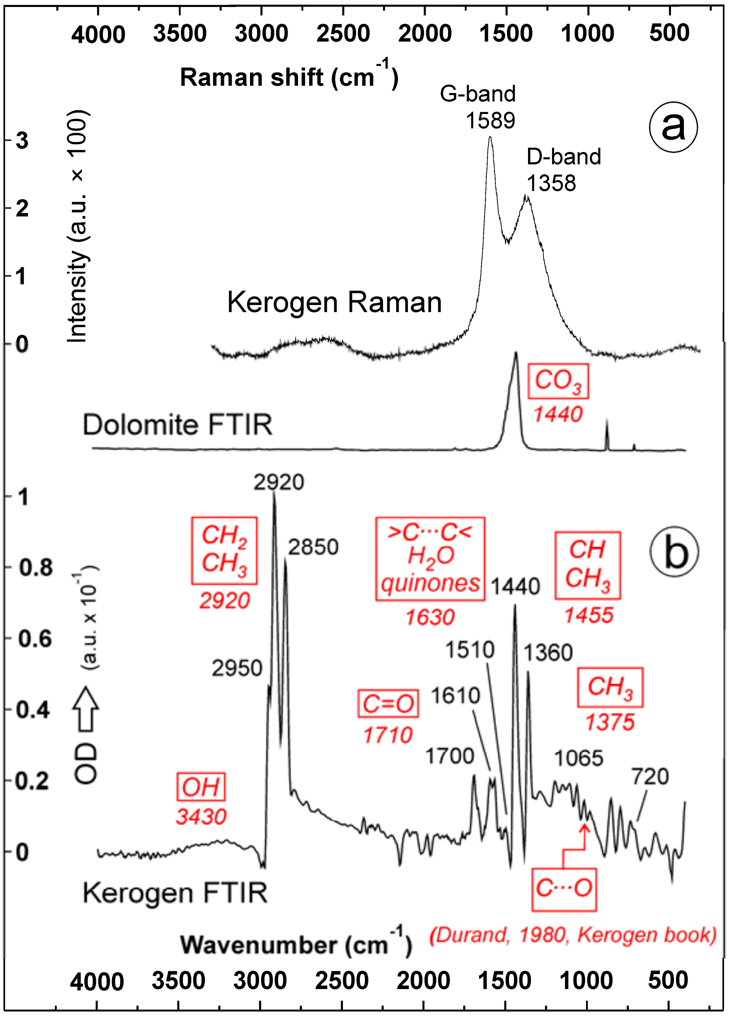

Figure 9.- Raman-PL and FTIR spectra of kerogen sample from Lodares (Soria, Spain).

Figure 9b displays the FTIR spectrum of the black kerogen with the following bands together with the associated spectral features following a classic review on kerogen [49] as follows: 3430 cm^{-1} (O–H stretching), 2920 cm^{-1} (aliphatic C–H stretching), 1710 cm^{-1} (C=O stretching in carboxyls), 1630 cm^{-1} “puzzle band” (aromatic C=C and olefinic groups, quinones, conjugated C=O groups, H_2O), 1455 cm^{-1} (aliphatic CH, CH_3 bending), 1375 cm^{-1} (CH_3), etc.; however some contribution of peaks attributable to dolomite carbonate cannot be disregarded, e.g., 1440 cm^{-1} and small peaks at ca. 880 and 720 cm^{-1} $(CO_3)^{2-}$. This section may be divided by subheadings. It should provide a concise and precise description of the experimental results, their interpretation as well as the experimental conclusions that can be drawn.

5.- Discussion

5.1.- Ore deposits of iron-manganese minerals

The Lodares area hosts a fossilized intra-Miocene geothermal field placed along an inferred geological fault. This deposit as well as other carbonate rock-hosted epithermal deposits could be interesting polymetallic sources. From a genetic point of view, in the Lodares area using EPMA, ESEM-EDS, ICPMS and XRD results is possible to infer the following processes: (1) pre-ore decalcification with dolostone removal and re-precipitation, (2) a silicification process associated with pyrite, (3) precipitation of galena and Hg-Tl-Sb-As sulfides, (4) late-stages of cinnabar and baryte in pockets; (5) oxide ore stage and carbonate alteration, e.g., complex Mn–Fe-rich oxy-hydroxides, arsenates, sulfates in residual leached rock and infill of karstic cavities. From a geochemical viewpoint, shallow epithermal ores often include different proportions of Au Ag, Te, Se, Hg, As, Sb and Tl suggesting geochemical cycles linked by their similar volatile behavior through subduction, partial melting in the mantle and late magma degassing processes [17]. **Figure 3** suggests that the hydrous dissolution which created the quartz pits could also remove former Tl clusters in quartz. Accordingly, Tl has occasionally been found locked in quartz masses in severely altered hydrothermal iron ores, mainly composed by goethite-lepidocrocite phases.

5.2.- Weathered hydrothermal paraganeses of pyrite-kerogen-thallium associations

The Lodares quarry outcrops a stockwork structure of pyrite-rich mineralized veins hosted in sedimentary dolostones. The close association among masses of sulfides (acid environment) hosted in dolostone (alkaline environment) facilitates chemical neutralization reactions leading to the formation of new hydrated phases such as gypsum, jarosite, scorodite, anglesite, epsomite, hexahydrite, melanterite, goethite and lepidocrocite. Basically, the host rock provides Ca and Mg after dissolution of dolostone and the hydro-oxidation of the iron sulfide veins (FeS_2) leaks out iron hydroxides and sulfate groups (SO_4^{2+}) to the environment. The XRD analyses show different mineral phases which can be interpreted as follows: (i) neo-formed epithermal phases such as pyrite, sphalerite, galena, baryte, (ii) inherited xenolithic grains removed from lower strata, such as quartz, muscovite and feldspars, (iii) host rock fragments, i.e., dolostone and finally (iv) secondary phases activated by hydration processes and redox reactions linked with epithermal fluids, atmospheric weathering, bacterial activity, producing, for instance, gypsum, jarosite, scorodite, anglesite, goethite, elemental sulfur, epsomite, etc., In the redox mechanisms we can infer oxidation of As from As^{1-} to As^{5+}, oxidation of S from S^{2-} in sulfides to S^0 in native sulfur, etc. Some weathering processes were accelerated by bacterial activity, since we identified bacterial textures by ESEM such as corrosion pits and micro-deposits of elemental sulfur. Lodares quarry also displays spill downstream paths of brown color sediments, starting from the pyrite masses obviously with a decreasing Tl concentration depending mainly on the pyrite weathering.

5.3.- EPMA and ICP-MS analyses of thallium-bearing samples

The ternary representation of Sb-As-Tl concentrations obtained from more than 100 EPMA spots in Lodares pyrite masses (Fig. 6) shows greater density near the As triangle end which is compatible with second-stage epithermal mineralization linked with precipitation of Pb-Hg-Tl-Sb-As sulfides hosted in dolostone rocks, similar to those of Agdarreh (Iran) [15] or Allchar (Macedonia) [50-53]. The observation of the ICP-MS analyses (Table 3) of samples from Lodares quarry (16 samples), Blocona (2 samples) quarry and other three Fe-Mn ore samples collected from Jubera, Velilla and Avenales quarries suggests the following comments on each element: Minor amounts of Na are reasonable in limestone and sulfide environments, however sample KERO (kerogen) contains 138 mg kg^{-1}, in addition to its strong polyalkyl structure, which supports the hypothesis of a hydrothermal kerogen formed from marine algal films. Magnesium-rich samples numbered from LD6 to LD10 retain partial amounts of the dolostone source. Minor amounts of aluminum probably associated to Buntsandstein sandstone silicates could be moved by ascent hydrothermal fluids. Minor amounts of potassium probably included in K-feldspar and muscovite are coming from the inward Buntsandstein sandstone grains transported by rising hydrothermal fluids. Calcium is abundant in all samples since host rocks are dolostones. Cadmium appears accessorily in all samples coupled to the abundant amount of Zn, furthermore, BLMN sample, i.e., pure MnO_2 from the Blocona quarry exhibits 6673 mg kg^{-1} of Cd which can be explained by geochemical affinity with Zn element during the hydrothermal processes, e.g., the isotypics pairs wurtzite-greenockite and sphalerite-hawleyite. Vanadium element is clearly coupled to the iron oxy-hydroxide masses. Chromium amount is low with the exception the kerogen (690 mg kg^{-1}). Manganese is very abundant in all iron ores as it was detected in the ICP-MS analyses. Iron (Fe) is the main element in pyrite and weathered minerals such as goethite and lepidocrocite. The elements Hf, Ni, Er, Be, Ho, Ag, are concentrated in Fe-Mn ores however Hg is most abundant in pyrite since it is easily leached during weathering processes. Thallium is a chalcophile element and primary associated to hydrothermal pyrite, as it is plainly observed in Table 3 (Tl/LD14 = 188 mg kg^{-1} and weathered pyritic sediments). The amount of Tl substituting K atoms in K-feldspar and K-micas is low since such minerals are accessorial in our iron ores. The hydrothermal kerogen exhibits 13 mg kg^{-1} of Tl, the Mn ore 27 mg kg^{-1} and the weathered hydrothermal goethite-lepidocrocite complexes shows 142 mg kg^{-1} (Jubera) and 273 mg kg^{-1} (Avenales). The amount of Tl in the Mn ores could be related to its geochemical behavior similar to those shown by K; it is well-known that the so-called "tunnel Mn oxides" are able to host K (and then Tl) in their tunnels (e.g., cryptomelane, $KMn^{4+}{}_7Mn^{3+}O_{16}$). In the weathered iron oxy-hydroxides masses, Tl is hosted in secondary sulfates (e.g., in jarosite).

Pb, Zn and Sb are abundant elements associated to the sulfide phases, e.g., pyrite remaining in the Fe ores and kerogen but not in the manganese oxides. Our analyses show also as uranium molybdenum, yttrium, and thallium are mainly coupled to kerogen masses in good agreement with the published classic geochemistry of black shale deposits [54].

5.4.- Molecular characteristics of the hydrothermal kerogen

The Raman-PL spectrum of the Lodares pyro-bitumen shows the typical peaks at 1589 cm^{-1} (G-band) and 1358 cm^{-1} (D-band) of carbonaceous materials. In resonance Raman spectra such D-modes are produced by disorder in *sp*^{2}-hybridized carbon systems. The peak at ca. of 1589 cm^{-1} (G-band) arises from stretching of C–C bonds in graphitic materials and they are shared to all sp2 carbon materials. In the Lodares kerogen case, the Raman spectrum also exhibits a broad band in the range 2500–2800 cm^{-1}. This so-called 2D(G*)-band is second-order two-phonon process associated with the G-band in *sp*^{2} carbonaceous materials. Raman spectroscopy is a sensitive technique analyzing disorder grades in *sp*^{2} carbon compounds. The general shape of the Raman spectrum from Lodares kerogen roughly fits on previously analyzed lignite international specimens of UK, Germany, USA, etc. [55]. In accordance with the FTIR spectrum (**Figure 8b**) the black kerogen sample collected in the Lodares quarry is strongly paraffinic in nature, with a low oxidation grade. Nevertheless, the spectrum suggests some aromatic structures at 1510 and 1620 cm^{-1} and carboxyl groups at 1720 cm^{-1}, but no hydroxyl groups at 3400 cm^{-1}. The whole spectrum does not look like common bitumen from peat or soil, which is oxidized. It probably was formed in aquatic or reducing environment: the overall aromatic content is low and no typical lignin signature was evident in the FTIR spectrum. There is also appreciated a diagnostic paraffinic band at ca. 720 cm^{-1} (polymethylene, >C4 chains) and other small bands between 400–800 cm^{-1} which could be due to organic, e.g., polycyclic aromatic or mineral constituents. Taking into account the dolostone host rock of the kerogen masses, we also included a dolomite FTIR spectrum with a maximum peak at 1440 cm^{-1}, accordingly, the large band at 1400 cm^{-1} and two sharp bands below 800 cm^{-1} of the kerogen spectrum could also be attributed to dolomite.

6.- A genetic model suggested for the thallium ore deposits of Lodares (Soria, Spain)

Both geological field exploration and samples analyses suggest a simplified genetic model outlined in **Figure 10**. The inward Paleozoic metapelite facies including sulfide mineralization was observed in neighboring areas surrounding the iron outcrops. It is important to explain a suitable origin of S. Secondly, a conceptual model of hydrothermal reservoir [56-58] could be applicable for meteoric water percolating through fissures deep into the whole formation coming in contact with heated rocks. Hot mineralized fluids containing H_2O and H_2S gases climb up across the Fe sandstone masses of the Buntsandstein formation facilitating the formation of polymetallic sulfides, mainly pyrite.

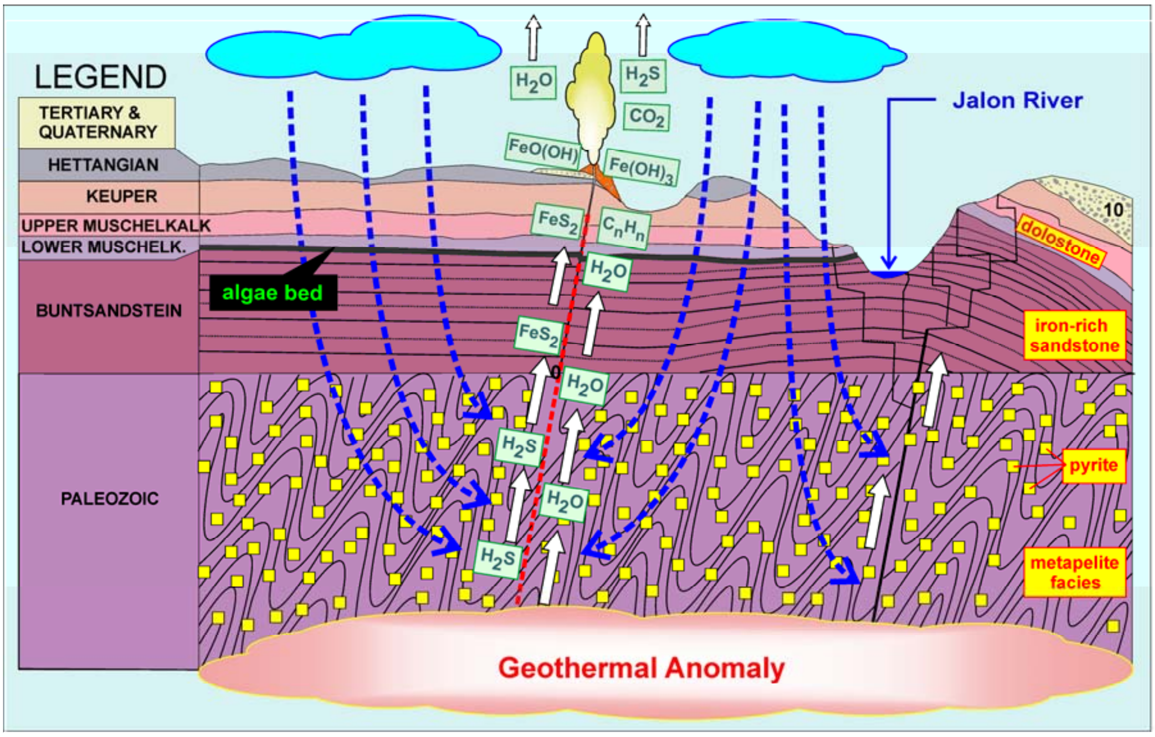

Figure 10.-Simplified sketch on the genetic model suggested for the thallium ore deposits of Lodares (Soria, Spain)

The Muschelkalk dolostone unit has intertidal episodes and development of algal tapestries which was surely remobilized by these hydrothermal hot waters forming the pyro-bitumen collected in the Lodares quarry veins together with neo-formed dolomite crystals and pyrite. The molecular analyses of the analyzed kerogen support such model. These Fe-Mn mineralizations were found hosted in Jurassic and Tertiary limestone facies which must be interpreted as formed in Tertiary or post-Tertiary times. Concerning the present day status of the mineral assemblages, they offer varied alteration grades from quite unaltered pyrite (Lodares quarry) up to large goethite-lepidocrocite masses in which the weathering ways of atmospheric waters are easily observed in the quarry front (Somaén-Velilla mine).

7.- Conclusions

The iron-manganese ores here studied are hosted in dolostone rocks sited along ca. 15 km of fossil thermal springs following a geological fault in the Lodares surroundings (Soria, Central Spain). The Tl-bearing samples were analyzed by environmental scanning electron microscopy and energy dispersive spectroscopy (ESEM-EDS), electron probe micro-analysis (EPMA), inductively coupled plasma-mass spectroscopy (ICP-MS), X-ray diffraction analysis (XRD), Tl LIII-edge X-ray absorption near-edge structure (XANES) spectroscopy, micro-Raman and photoluminescence analysis (Raman-PL), Fourier transform infrared spectroscopy (FTIR) to explore the Tl behavior in both epithermal and weathered phases.

Hydrothermal pyrite is an important source of thallium but this element was also detected in secondary iron goethite, lepidocrocite pyrolusite and jarosite ores, associated hydrothermal kerogen, accessorial potassium minerals (orthoclase, muscovite) and tiny Tl-bearing clusters shielded in quartz masses. We also detected accessorial Tl, Sb, Hg, Pb, As and Ba elements in the weathered iron ores since they are characteristic parageneses in massive iron sulfide phases formed in the same volcano hydrothermal processes.

Epithermal phases found in the Lodares quarry are pyrite, sphalerite, galena and baryte while secondary phases are gypsum, jarosite, scorodite, anglesite, goethite, epsomite and elemental sulfur produced by both hydroxylation and bacterial processes. Thallium contents are associated to hydrothermal pyrite (200 mg kg^{-1}), kerogen (13 mg kg^{-1}), manganese ores (27 mg kg^{-1}) and iron hydroxides and sulphates (142 mg kg^{-1}).

The Tl-bearing Fe-Mn ores formation follow a conceptual model of hydrothermal reservoir in which meteoric water percolates deep through fissures into the whole formation coming in contact with heated rocks. Hot mineralized fluids with H_2O and H_2S gases climb up across underneath iron-sandstone masses promoting nucleation of polymetallic sulfides, mainly pyrite. The Lodares outcrops exhibit interesting details on Tl geochemical cycle bound to a frame of epithermal formation of pyrite and remobilized kerogen.

Acknowledgments: This work was funded under the Spanish National Plan for Scientific and Technical Research and Innovation through the project CTM2014-55321-P.

Conflicts of Interest: The authors declare no conflict of interest.

Author Contributions: Authors Javier Garcia-Guinea, Paula Lopez-Arce and Fernando Garrido performed field work, mineralogical and chemical analyses and ore geology models. Andreas Voguelin and Fernando Garrido studied the thallium-bearing particles to be framed in the weathering models. Gonzalo Almendros performed laboratory driven experimental on kerogen and organic samples by ATR-FTIRT and Andreas Voguelin, Jörg Göttlicher and Stephan Mangold examined several thallium-bearing samples by Tl LIII-edge X-ray absorption near-edge structure (XANES) spectroscopy.

References

[1] Coggon, R. M.; Rehkämper M. ; Atteck C. ; Teagle D. A. H.;. Alt J. C; and Cooper M. J. Controls on thallium uptake during hydrothermal alteration of the upper ocean crust. *Geochim. Cosmochim. Acta.* **2014)**, 144, 25–42. DOI:10.1016/j.gca.2014.09.001.

[2] D'Orazio; M., Biagioni C.; Dini A.; and Vezzoni S. Thallium-rich pyrite ores from the Apuan Alps; Tuscany, Italy: constraints for their origin and environmental concerns, *Miner. Deposita* **2016,** 52, 1–21, DOI:10.1007/s00126-016-0697-1.

[3] Gomez-Gonzalez, M. A.; Garcia-Guinea J., Garrido F.; Townsend P. D.; and Marco J. F. Thallium and manganese complexes involved in the luminescence emission of potassium-bearing aluminosilicates, *J. Lumin*, **2015,** 159, 197–206, DOI:10.1016/j.jlumin.2014.11.011.

[4] Hettmann; Kreissig K.; Rehkämper M.; Wenzel T.; Mertz-Kraus R.; and Markl G. Thallium geochemistry in the metamorphic Lengenbach sulfide deposit, Switzerland: Thallium-isotope fractionation in a sulfide melt. *Am. Mineral.* **2014**, 994, 793–803, DOI:10.2138/am.2014.4591.

[5] Nielsen, S. G.; Klein F.; Kading T.; Blusztajn J.; and Wickham K. Thallium as a tracer of fluid-rock interaction in the shallow Mariana forearc, *Earth Planet. Sc. Lett.* **2015,** 430, 416-426. DOI:10.1016/j.epsl.2015.09.001.

[6] Xiong, Y. Hydrothermal thallium mineralization up to 300°C: A thermodynamic approach, *Ore Geol. Rev.* **2007,** 32(1–2), 291–313, DOI:10.1016/j.oregeorev.2006.10.003.

[7] Zhou T. F.; Fan Y., Yuan F.; Wu M. A.; Hou M. J.; Voicu G.; Hu Q. H.; Zhang Q. M.; and Yue S. C. A preliminary geological and geochemical study of the Xiangquan thallium deposit, eastern China: The world's first thallium-only mine, *Miner. Petrol.* **2005,** 85, 243–251, DOI:10.1007/s00710-005-0088-2.

[8] López Antón M.A; Spears D. A.; Diez Somoano M.; and Martínez Tarazona M. R. Thallium in coal: Analysis and environmental implications, *Fuel* **2013)**, 105, 13–18, DOI:10.1016/j.fuel.2012.08.004.

[9] Dai S.; Zeng R.; and Sun Y. Enrichment of arsenic, antimony, mercury, and thallium in a Late Permian anthracite from Xingren, Guizhou, Southwest China, *Int J Coal Geol* **2006**, 66(3), 217–226, DOI:10.1016/j.coal.2005.09.001.

[10] Karbowska B., Presence of thallium in the environment: sources of contaminations, distribution and monitoring methods, *Environ Monit Assess* **2016,** 188(11) 640, DOI:10.1007/s10661-016-5647-y.

[11] Lopez-Arce; P., Garcia-Guinea J. and Garrido F. Chemistry and phase evolution during roasting of toxic thallium-bearing pyrite, *Chemosphere* **2017,** 181, 447–460, DOI:10.1016/j.chemosphere.2017.04.109.

[12] Sturini M.; Maraschi F.; Cucca L.; Spini G.; and Profumo A. Determination of Inorganic Thallium Compounds in the Particulate Matter of Emissions and Workplace Air by Sequential Dissolution, *Anal. Sci.* **2009,** 25, 121–124, DOI:10.2116/analsci.25.121.

[13] Vaněk A.; Grosslova Z.; Mihaljevič M.; Ash C., Isotopic Tracing of Thallium Contamination in Soils Affected by Emissions from Coal-Fired Power Plants, *Environ. Sci. Technol.* **2016,** 50, 9864–9871, DOI:10.1021/acs.est.6b01751.

[14] Xiao T.; Guha J.; and Boyle D. High thallium content in rocks associated with Au-As-Hg-T1 and coal mineralization and its adverse environmental potential in SW Guizhou, China. *Geochem-Explor. Env. A* **2004,** 4, 243-252, DOI:10.1144/1467–7873/04-204.

[15] Johan, Z.; Mantienne, J. Thallium mineralization at Jas Toux, Hautes-Alpes, France: a complex epithermal, sediment-hosted, ore forming system. *J. Czech Geol. Soc.* **2000,** 45, 63-77.

[16] Kochneva N.T.; Volkov, A. V.; Serafimovski T.; Tasev G.; Tomson; I.N. Tectonic position of the Alshar Au-As-Sb-Tl deposit, Macedonia. *Dokl. Earth Sci.,* **2006,** 407, 175–178. DOI: 10.1134/S1028334X06020036.

[17] Daliran F. The carbonate rock-hosted epithermal gold deposit of Agdarreh, Takab geothermal field, NW Iran – Hydrothermal alteration and mineralisation, *Miner. Deposita.* **2008**, 43, 383-404, DOI:10.1007/s00126-007-0167-x.

[18] Huang; J.; X. Chu; G. Jiang; L. Feng; and H. Chang (2011), Hydrothermal origin of elevated iron, manganese and redox-sensitive trace elements in the c. 635 Ma Doushantuo cap carbonate. *J. Geo. Soc.*, **2011,** 168, 805-816, doi:10.1144/0016-76492010-132.

[19] Saunders J. A., Textural evidence of episodic introduction of metallic nanoparticles into bonanza epithermal ores, *Minerals* **2012,** 2, 228–243, DOI:10.3390/min2030228.

[20] Saunders J. A.; Unger D. L.; Kamenov G. D.; Fayek M.; Hames W. E.; and Utterback W. C. Genesis of middle miocene yellowstone hotspot-related bonanza epithermal Au-Ag deposits, Northern Great Basin, USA, *Miner Deposita* **2008,** 43(7), 715–734, DOI:10.1007/s00126-008-0201-7.

[21] Fan Y.; Zhou T.; Yuan F.; and Wu M. Geological and geochemical constraints on the genesis of the Xiangquan Tl-only deposit, eastern China, *Ore Geol. Rev.* **2014,** 59, 97–108, DOI:10.1016/j.oregeorev.2013.12.008.

[22] Murakami H.; Hattori W.; Mizomata Y.; and Aoki R. Tunneling observation of Tl quasi-localized impurity states in superconductive semiconductor Pb(Tl)Te, *Physica C* **1996,** 273, 41–48.

[23] Bauman W. A.; Raza M.; Chayes Z. and Machac J. Tomographic thallium-201 myocardial perfusion imaging after intravenous dipyridamole in asymptomatic subjects with quadriplegia, *Arch. Phys. Med. Rehab.* **1993,** 74, 740–744, DOI:10.1016/0003-9993(93)90036-A.

[24] Kassis, A. I., Adelstein S. J., Haydock C., and Sastry K. S. R., Thallium-201: An experimental and a theoretical radiobiological approach to dosimetry. *.J Nucl. Med.* **1983**, 24, 1164–1175.

[25] Horn P.; Schmid A.; and Brãžunlich P. Photoacoustic observation of third-order absorption in thallium halides at 1.06 µm, *IEEE J. Quantum. Electron.*, **1983,** 19, 1169–1172, DOI:10.1109/JQE.1983.1072003.

[26] Kaufman R. G.; Hadley W. B.; and Hersh H. N. The scintillation mechanism in thallium doped alkali halides, *IEEE Trans. Nucl. Sci.* **1970,** 17, 82–88, DOI:10.1109/TNS.1970.4325679.

[27] Červeny L., Paseka I., Tobola S., and Ružička V. Hydrogenation of 2,5-dimethyl-2,4-hexadiene and cis-2-heptene on palladium black modified by lead, thallium and cadmium, *J. Chem. Technol. Biotechnol.* **1986,** 36, 144–151, DOI:10.1002/jctb.280360307.

[28] Gaikwad A., Transport of indium, gallium and thallium metal ions through chromatographic fiber supported solid membrane in acetylacetone containing mixed solvents, *Chinese J. Chem. Eng.* **2011,** 19, 955–963, DOI:10.1016/S1004-9541(11)60077-3.

[29] Hitomi K.; Muroi O.; Shoji T.; Suehiro T. and Hiratate Y. Room temperature X- and gamma-ray detectors using thallium bromide crystals. *Nucl. Instrum. Meth. A* **1999,** 436, 160–164. DOI:10.1016/S0168-9002(99)00614-2.

[30] UrRahman I; Fisher W. A.; Hofstadter R.; and Jing S. Behavior of thallium bromide conduction counters, *Nucl. Instrum. Meth. A* **1987,** 261(3), 427–439. DOI:10.1016/0168-900287)90350-0.

[31] Jacobson A. R.; McBride M. B.; Baveye P.; and Steenhuis T. S. Environmental factors determining the trace-level sorption of silver and thallium to soils, *Sci. Total. Environ.* **2005,** 345, 191–205. DOI:10.1016/j.scitotenv.2004.10.027.

[32] Peter A. L. J. and Viraraghavan T. Thallium: A review of public health and environmental concerns. *Environ. Int.* **2005**, 31, 493–501. DOI:10.1016/j.envint.2004.09.003.

[33] Xiao T.; Boyle D., Guha J.; Rouleau A.; Hong Y. and Zheng B. Groundwater-related thallium transfer processes and their impacts on the ecosystem: Southwest Guizhou Province, China. *Appl. Geochem.* **2003**, 18, 675–691. DOI:10.1016/S0883-2927(02)00154-3.

[34] Zhou T.; Fan Y.; Yuan F.; Cooke D.; Zhang X.; and Li L. A preliminary investigation and evaluation of the thallium environmental impacts of the unmined Xiangquan thallium-only deposit in Hexian, China. *Environ. Geol.* **2008**, 54, 131–145, DOI:10.1007/s00254-007-0800-0.

[35] Rasmussen B. and Buick R. Oily old ores: Evidence for hydrothermal petroleum generation in an Archean volcanogenic massive sulfide deposit, *Geology* **2000**, 28, 731–734. DOI:10.1130/0091-7613(2000)28<731:OOOEFH>2.0.CO;2.

[36] Cody G. D. Transition metal sulfides and the origins of metabolism, *Annu. Rev. Earth. Pl. Sc.* **2004**, 32, 569–599, DOI:10.1146/annurev.earth.32.101802.120225.

[37] Ferry J. G. and House C. H. The stepwise evolution of early life driven by energy conservation, *Mol. Biol. Evol.*, **2006,** 23, 1286–1292. DOI:10.1093/molbev/msk014.

[38] Williams R. J. P. The natural selection of the chemical elements, *Cell. Mol. Life Sci* .**1997,** 53, 816–829. DOI:10.1007/s000180050102.

[39] Tavani S.; Quintà A.; and Granado P. Cenozoic right-lateral wrench tectonics in the Western Pyrenees (Spain): The Ubierna Fault System, *Tectonophysics* **2011,** 509, 238–253. DOI:10.1016/j.tecto.2011.06.013.

[40] López-Gómez J.; Mas R. and Arche A. The evolution of the Middle Triassic (Muschelkalk) carbonate ramp in the SE Iberian Ranges, eastern Spain: sequence stratigraphy, dolomitization processes and dynamic controls, *Sedim. Geol.* **1993,** 87, 165–193. DOI:10.1016/0037-0738(93)90003-N.

[41] Soria A. R.; Liesa C. L.; Rodríguez-López J. P.; Meléndez N.; DeBoer P. L and Meléndez A. An Early Triassic evolving erg system (Iberian Chain, NE Spain): Palaeoclimate implications, *Terra Nova* **2011**, 23, 76–84, DOI:10.1111/j.1365-3121.2011.00986.x.

[42] Dumas S. and Arnott R. W. C. Origin of hummocky and swaley cross-stratification - The controlling influence of unidirectional current strength and aggradation rate, *Geology* **2006,** 34, 1073–1076. DOI:10.1130/G22930A.1.

[43] Eyles N. and Clark B. M. Significance of hummocky and swaley cross-stratification in late Pleistocene lacustrine sediments of the Ontario basin, Canada, *Geology* **1986,** 14, 679–682. DOI:10.1130/0091-7613(1986)14<679:SOHASC>2.0.CO;2.

[44] Rosenfeld A. and Wu A. Y. Parallel computers for region-level image processing. *Pattern Recogn.* **1982**, 15, 41–50, DOI:10.1016/0031-3203(82)90059-0.

[45] Voegelin, A., Pfenninger, N., Petrikis, J., Majzlan, J., Plötze, M., Senn, A.-C., Mangold, S., Steininger, R. and Göttlicher, J. Thallium speciation and extractability in a thallium- and arsenic-rich soil developed from mineralized carbonate rock. *Environ. Sci. Technol.* **2015,** 49, 5390-5398. DOI: 10.1021/acs.est.5b00629.

[46] Dutrizac, J.E., Chen, T.T. and Beauchemin, S. The behaviour of thallium(III) during jarosite precipitation. *Hydrometallurgy.* **2005** 79, 138-153. doi.org/10.1016/j.hydromet.2005.06.003.

[47] Ravel, B. and Newville, M. ATHENA, ARTEMIS, HEPHAESTUS: data analysis for X-ray absorption spectroscopy using IFEFFIT. *J. Synchrotron Rad*. **2005**, 12, 537-541. DOI: 10.1107/S0909049505012719

[48} Liu, W. and Zhang, X. Experimental study of microbial pyrite oxidation: a suggestion for geologically useful biosignatures. *Geomicrobiol Jour.* **2015** 32, 466–47. DOI10.1080/01490451.2014.942446

[49] Durand, B. Kerogen: insoluble organic matter from sedimentary rocks. Paris : Editions Technip, **1980**. 519 p. http://trove.nla.gov.au/work/10153439. ISBN 2710803712

[50] Radtke, A.S., Dickson F.W., and J.F. Slack Occurrence and formation of avicennite, Tl_2O_3, as a secondary mineral at the Carlin gold deposit, Nevada. Handbook of mineralogy of the *J. Res. U.S. Geol. Surv*. **1978,** 6, 241-246.

[51] Balič Žunić, T., Moëlo, Y., Lončar, Ž. and Micheelsen, H. (1994) Dorallcharite, $Tl_{0.8}K_{0.2}Fe_3(SO_4)_2(OH)_6$, a new member of the jarosite-alunite family. Eur. J. Miner **1993** 6, 255-263. DOI: 10.1127/ejm/6/2/0255.

[52] Bačeva K.; T. Stafilov; R. Šajn; C. Tănăselia and Makreski P. Distribution of chemical elements in soils and stream sediments in the area of abandoned Sb-As-Tl Allchar mine, Republic of Macedonia. *Environ. Res.* **2014,** 133, 77–89, DOI:10.1016/j.envres.2014.03.045.

[53] Jankovic S. Allchar Tl-As-Sb deposit, Yugoslavia and its specific metallogenic features, *Nucl. Instrum. Meth. A.* **1988,** 271, 286–286. DOI 10.1016/0168-9002(88)90170-2

[54] Vine J.D.; Tourtel, E.B. Geochemistry of black shale deposits - A summary report *Econ. Geol.* **1970,** 65, 253-272. DOI:10.2113/gsecongeo.65.3.253

[55] Kostova I.; Tormo L.; Crespo-Feo E. and García-Guinea J. Study of coal and graphite specimens by means of Raman and cathodoluminescence, *Spectrochim. Acta A* **2012,** 91, 67–74. DOI:10.1016/j.saa.2012.01.056.

[56] Lee S. W.; Dong G. and Rey J. Interpreting the structural characteristics of underground natural flows to determine the productivity potential of hydrothermal reservoirs. *Geothermal Res. Council Trans.* **2011,** 35, 1581–1588. ISSN: 0193-5933; ISBN: 0-934412-96-0.

[57] Ostermann I. Three-dimensional modeling of heat transport in deep hydrothermal reservoirs, *GEM Int. J. Geomath.* **2011,** 2(1), 37–68, DOI:10.1007/s13137-011-0017-y.

[58] White D. E. Diverse origins of hydrothermal ore fluids, *Econ. Geol*, **1974,** 69, 954–973. DOI:10.2113/gsecongeo.69.6.954.